

RESEARCH

Open Access



Biocompatible copper formate-based nanoparticles with strong antibacterial properties for wound healing

Yue Zhou^{1,2}, Ping Sun^{1,2}, Yongbin Cao^{1,2}, Jiahao Yang^{1,3}, Qingzhi Wu^{1,2,3*} and Jian Peng^{1,2,3*}

Abstract

Copper-based antibacterial materials have emerged as a potential alternative for combating bacterial infections, which continue to pose significant health risks. Nevertheless, the use of copper-based nanoparticles as antibacterial agents has faced challenges due to their toxicity towards cells and tissues. To overcome this obstacle, we propose a new approach using a contact-active copper-based nanoparticles called polydopamine (PDA)-coated copper-amine (Cuf-TMB@PDA). The positively charged surface of Cuf-TMB@PDA enables efficient targeting of negatively charged bacteria, allowing controlled release of Cu(II) into the bacterial cell membrane. Moreover, Cuf-TMB@PDA exhibits similar ·OH signals as Cuf-TMB suspensions in previous work. In cytotoxicity assays conducted over 72 h, Cuf-TMB@PDA demonstrated an efficacy of 98.56%, while releasing lower levels of Cu(II) that were less harmful to cells, resulting in enhanced antimicrobial effects. These antimicrobial properties are attributed to the synergistic effects of charge-contact activity of PDA, controlled release of Cu(II), and free radicals. Subsequent in vivo experiments confirmed the strong antimicrobial potency of Cuf-TMB@PDA and its ability to promote wound healing.

Keywords Cuf-TMB@PDA, Bioactive, Antibacterial, ·OH radical, Wound healing

Introduction

Microbiologically induced diseases which could disseminated through the food chain, pose substantial hazards and financial burdens to human society [1–3]. Pathogenic microorganisms like *Escherichia coli* (*E. coli*), *Staphylococcus aureus* (*S. aureus*), and others have been linked to various infections, including wound infections,

bloodstream infections, and systemic infections [4–10]. The rise of antibiotic-resistant bacteria rendered conventional antibiotic treatments are no longer effective at completely eradicating these illnesses [11–13]. Therefore, eliminating superbugs and addressing bacterial drug resistance have become crucial research areas in the biomedical field. Historically, metals such as gold [14], silver [15, 16], copper [17, 18], and zinc [19] have been utilized as antibacterial agents in various fields, including medicine and environmental studies [20–23]. Among them, copper possesses antimicrobial properties comparable to those of silver [24, 25], and serves as an essential co-factor for organisms, promoting vital processes such as vascular growth, collagen deposition, and wound re-epithelialization [26, 27]. Nevertheless, copper can be detrimental when its amount exceeds the threshold

*Correspondence:

Qingzhi Wu
wuqzh@whut.edu.cn

Jian Peng
jianpeng@whut.edu.cn

¹State Key Laboratory of Advanced Technology for Materials Synthesis and Processing, Wuhan 430070, China

²School of Chemistry, Chemical Engineering and Life Science, Wuhan University of Technology, Wuhan 430070, China

³School of Material Science and Engineering, Wuhan University of Technology, Wuhan 430070, China



© The Author(s) 2023. **Open Access** This article is licensed under a Creative Commons Attribution 4.0 International License, which permits use, sharing, adaptation, distribution and reproduction in any medium or format, as long as you give appropriate credit to the original author(s) and the source, provide a link to the Creative Commons licence, and indicate if changes were made. The images or other third party material in this article are included in the article's Creative Commons licence, unless indicated otherwise in a credit line to the material. If material is not included in the article's Creative Commons licence and your intended use is not permitted by statutory regulation or exceeds the permitted use, you will need to obtain permission directly from the copyright holder. To view a copy of this licence, visit <http://creativecommons.org/licenses/by/4.0/>. The Creative Commons Public Domain Dedication waiver (<http://creativecommons.org/publicdomain/zero/1.0/>) applies to the data made available in this article, unless otherwise stated in a credit line to the data.

established by longstanding evolutionary homeostatic mechanisms.

Considerable research efforts have been focused on strategies aimed at reducing the utilization of copper or mitigating its release rate [24, 28–30]. For instance, Ameer and colleagues utilized folic acid as a stabilizing agent for copper metal-organic frameworks (Cu-MOFs), resulting in a decrease in their degradation rate and the release rate of Cu(II) ions. This approach effectively alleviated the harmful toxic effects associated with Cu(II) ions [25]. Du et al. proposed a methodology for incorporating silver onto Poly-Cu MOFs, resulting in a lower copper node density and a higher loading of Ag NPs. This approach led to a reduced release of Cu(II) ions and an enhanced release of Ag(I) ions, ultimately improving biocompatibility and heightening antimicrobial properties [28]. Furthermore, various biocompatible nanomaterials, including polydopamine [31, 32], chitosan [33], carbon quantum dots [34], tannic acid [35] and their derivatives [36, 37], have been developed as effective ligands for copper complexes [38–40]. The coordination of copper with these ligands not only results in a reduction in copper content, but also allows for synergistically harnessing of their properties, achieving a more potent sterilization effect and enhanced biocompatibility. Boocaccini et al. formulated a biodegradable zein/CuBG that releases Cu(II) under physiological conditions, inducing oxidative stress in bacteria and effectively inhibiting their growth [40]. Zhang et al. introduced Cu_xO-PDA, a composite that instigated DNA degradation, lipid peroxidation, and the eradication of biofilms. This composite demonstrated effective bacteriostatic properties against both *E. coli* and *S. aureus* [41]. Despite the abundance of reports on copper-based antimicrobial materials, the development of copper-based materials that possess both cytocompatibility and strong antimicrobial properties have been relatively limited until now.

Herein, polydopamine-coated Cuf-TMB (Cuf-TMB@PDA) nanoparticles were designed and utilized to investigate their antimicrobial properties against two representative bacterial strains for wound healing. Catechol groups present on polydopamine demonstrate superior adhesion and compatibility with cells and tissues. Additionally, this positively charged PDA layer can adsorb onto the negatively charged bacterial cell membrane surface through electrostatic interactions, thus impeding bacterial nutrient uptake. Furthermore, it was demonstrated that Cuf-TMB@PDA exhibited signals of hydroxyl radicals ($\cdot\text{OH}$) in its electron spin resonance (ESR) spectrum. Due to the significant aggregation of Cuf-TMB@PDA on bacterial surfaces, gradual release of Cu(II), and damage caused by $\cdot\text{OH}$ within a specific range, the antibacterial efficacy of Cuf-TMB@PDA is significantly enhanced. Importantly, the obtained Cuf-TMB@PDA

not only exhibited effective antibacterial activity in vitro experiments but also demonstrated good biocompatibility. Subsequent in vivo experiments further confirmed the enhanced antibacterial effect of Cuf-TMB@PDA against *S. aureus*, as well as its more pronounced effect on skin wound healing.

Experimental section

Materials

Copper formate tetrahydrate (Cuf) and dopamine were purchased from Macklin Biochemical Co., Ltd (Shanghai, China). 3,3',5,5'-Tetramethylbenzidine and sodium chloride were obtained from J&K Scientific (Beijing, China). *Escherichia coli* (*E. coli*) and *Staphylococcus aureus* (*S. aureus*) were purchased from Shanghai Luwei Technology Co., Ltd (Shanghai, China). Mice dermal fibroblasts were obtained from Bena Culture Collection (Beijing, China). L929 cells were cultured in Dulbecco's modified Eagle's medium (DMEM, glucose concentration: 4.5 g L⁻¹) containing 10% FBS, 100 unit mL⁻¹ penicillin G sodium, and 100 μg mL⁻¹ streptomycin sulfate. All cells were maintained in an incubator at 37 °C in a humidified environment with 5% CO₂ in the air. Cell counting kit-8 (CCK-8) was obtained by the biosharp Co., Ltd (Guangzhou, China). Healthy Mice (Bablc/6) were obtained from Hubei Laboratory Animal Research Center (Wuhan, China). 5,5-dimethyl-1-pyrroline-n-oxide (DMPO) was purchased from Dojindo Molecular Technology Co., Ltd (Tokyo, Japan). The ultrapure water used in all experiments was made by passing through an ultrapure purification system (Ulupure, UPH-I-10TN). The animal protocols were approved by the Institutional Animal Care and Use Committee (IACUC) of Wuhan University of Technology.

Synthesis of the Cuf-TMB@PDA

The preparation of the Cuf-TMB nanoparticles was followed to our previous work [42]. For the synthesis of Cuf-TMB@PDA, dopamine (DA) solution (0.1 μg mL⁻¹) was mixed with Cuf-TMB suspension (78 μg mL⁻¹) in equal volumes under stirring at 380 rpm for 80 min at room temperature. This suspension was subsequently dialyzed for 48 h to remove any unreacted reagent and ions. The Cuf-TMB@PDA was freeze-dried and stored at 4 °C until further use.

Characterization

The crystal structure of the Cuf-TMB@PDA samples was examined by X-ray diffraction (XRD, Rigaku Smart Lab). The morphological characterization of the prepared samples was obtained by scanning electron microscopy (SEM, HITACHI SU8010), transmission electron microscopy (TEM, JEM-1400), and high-resolution TEM (HRTEM, Thermo Scientific Talos F200X G2). The

molecular structure and bond information of Cuf-TMB@PDA were obtained with Fourier transform infrared spectroscopy (FT-IR, Nicolet 6700) and laser confocal micro-Raman spectroscopy (Xplora PLUS). The composition and chemical state of the elements were characterized using X-ray photoelectron spectroscopy (XPS, Thermo Fisher Scientific K-Alpha+). The peroxidase-like (POD) activity of Cuf-TMB NPs was tested by UV-1900i Visible-near-infrared spectrophotometer (Shimadzu, Japan).

In vitro antibacterial property of Cuf-TMB@PDA

E. coli and *S. aureus* were chosen as the representative to evaluate the antibacterial activity of Cuf-TMB@PDA. These bacteria were incubated in liquid Luria-Bertani (LB) culture medium by shaking at 37 °C for 18 h. The optical density (OD) values of *E. coli* or *S. aureus* suspension were optimized at 0.3. Then, *E. coli* or *S. aureus* suspensions (500 μL) were incubated with Cuf-TMB@PDA, Cuf-TMB, and PBS (control group) at 37 °C, respectively. After 24 h, the live/dead staining cells of bacterial cells was determined using the microscope. The morphology was observed using SEM.

In vitro biocompatibility evaluation of Cuf-TMB@PDA

The cytocompatibility of Cuf-TMB@PDA was evaluated by the standard CCK-8 method. L929 cells were cultured for a further 24 h with various Cuf-TMB@PDA concentrations (0.001–63 $\mu\text{g mL}^{-1}$). 100 μL of fresh cell culture medium and 10 μL of CCK-8 solution were successively added to each well after washing with PBS. A microplate reader was used to measure the absorbance of each well at 495 nm after 4-hour incubation. The cell viabilities were expressed by the following equation:

$$\text{Cell Viability (\%)} = \left(\frac{A_1}{A_0} \right) \times 100\% \quad (1)$$

Where A_1 and A_0 represented the absorbance value of the experimental and control groups.

Live/dead cell staining assays, cells were exposed to medium-diluted Cuf-TMB@PDA for 24 h. Cells without Cuf-TMB@PDA treatment served as the control group. Subsequently, live/dead staining was applied to the cell mixture, followed by an incubation period. The stained L929 fibroblasts were subsequently examined using an inverted fluorescence microscope.

In vivo wound closure evaluation of the Cuf-TMB@PDA

The wound-healing performance of Cuf-TMB@PDA was evaluated utilizing a full-thickness rat skin incision model with certain modifications from previously reported methods [41]. All animal experiments received approval from the Institutional Review Board of Wuhan University of Technology. The infected wounds were divided into

three groups: PBS, Cuf-TMB, and Cuf-TMB@PDA. At specific intervals, namely, on days 3, 5, and 7 post-treatment, the wound size and body weight of the mice were recorded.

The wound closer ratio was calculated by the following formula:

$$\text{Wound concentration area (\%)} = \frac{\text{Area}_{0\text{day}} - \text{Area}_{n\text{day}}}{\text{Area}_{0\text{day}}} \times 100\% \quad (2)$$

In vivo histological analysis and toxicity assessment

At the completion of the wound healing experiment, the infected wound tissues and major organs of the mice were fixed in a 10% formalin solution for 24 h. Following ethanol dehydration, the tissues underwent paraffin embedding and were then sliced into 5 μm sections, subsequently stained with hematoxylin and eosin (H&E). The organ slices were observed using an Olympus FV1200 microscope. Blood samples were collected from the different treatment mice post in vivo wound healing experiment for subsequent biochemical analysis.

Results and discussions

Preparation and characterization of the Cuf-TMB@PDA

The typical synthetic procedure of the Cuf-TMB@PDA is schematically elucidated in Fig. 1. In this study, dopamine polymerization can be triggered by the presence of $\cdot\text{OH}$ and $\cdot\text{CHO}$ within the Cuf-TMB system (Scheme S1). Polydopamine (PDA) and Cuf-TMB were employed to fabricate a biocompatible and effective nanoparticle, as confirmed by the Raman spectra (Fig. 2a) and Transform Infrared spectroscopy (FT-IR) spectra (Fig. S1, Table S1). The Raman characteristic peaks at 474, 563 and 1085 cm^{-1} were assigned to trimethylammonium groups, $-\text{NH}$, and $-\text{CH}_2$ groups [43, 44], respectively. The zeta potential of Cuf-TMB was shifted from 4.98 to 27.25 mV after PDA coating (Fig. 2b, Fig. S2), indicating the successful formation of Cuf-TMB@PDA.

Furthermore, the XRD pattern of the synthesized Cuf-TMB@PDA exhibited an amorphous nature, consistent with the amorphous state observed in both Cuf-TMB and PDA (Fig. S3). High-angle annular dark-field scanning transmission electron microscopy (HAADF-STEM) images depicted an amorphous structure, with no noticeable boundary between the core and shell (Fig. S4). Simultaneously, a uniform and tightly adhered polydopamine (PDA) layer, approximately 10 nm thick, was consistently observed, intricately covering the spherical surface of Cuf-TMB. This observation indicates a robust binding between PDA and Cuf-TMB. Furthermore, the sizes of both Cuf-TMB and Cuf-TMB@PDA, as determined through

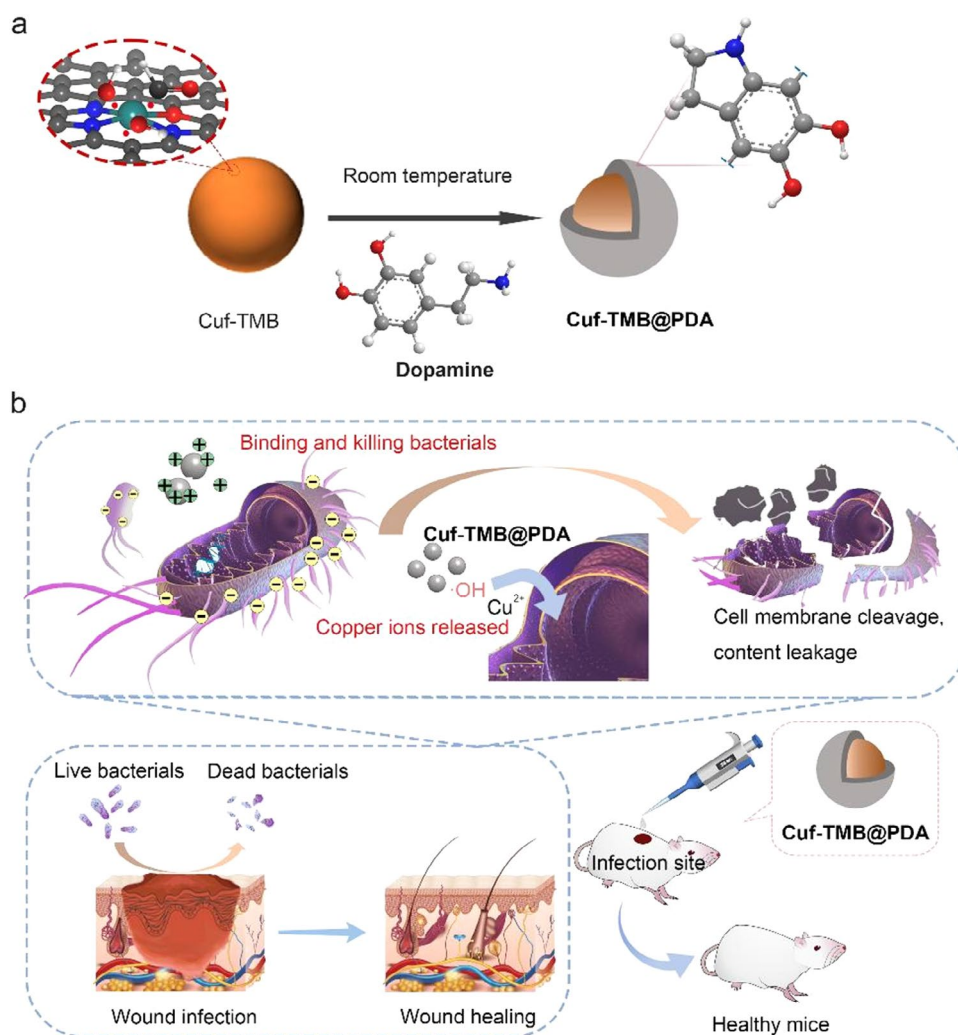


Fig. 1 Schematic illustration of the design and synthesis of the antimicrobial Cuf-TMB@PDA for promoting skin wound healing. **(a)** The synthetic pathway of Cuf-TMB@PDA; **(b)** Schematic representation depicting the antimicrobial attributes and wound-healing promotion of Cuf-TMB@PDA. The Cuf-TMB@PDA composite demonstrates potent antimicrobial characteristics well-suited for enduring *in vivo* antimicrobial interventions and improved wound healing

TEM images, were in good accordance with the size distribution assay (Fig. 2c and d, and Fig. S5). The energy-dispersive X-ray (EDX) mapping showed that Cu element was concentrated in the center of the nanoparticle, while O, N and C elements dispersed across the image area. An interesting observation was the distinct oxygen distribution pattern compared to Cuf-TMB, where oxygen was primarily located at the particle edges (Fig. 2e and f, and Fig. S6). This discrepancy can be attributed to the oxidation of dopamine into polydopamine (PDA) catalyzed by radicals from Cuf-TMB suspensions. Elemental analysis (Table S2) further provides conclusive evidence for the successful synthesis of Cuf-TMB@PDA.

The surface composition and valence states of each element in Cuf-TMB@PDA were characterized using X-ray photoelectron spectroscopy (XPS) technique

(Fig. 3). Analysis of the survey spectrum indicated the presence of predominant elements including copper (Cu), nitrogen (N), carbon (C), and oxygen (O) in Cuf-TMB@PDA (Fig. 3a). Decomposition of the Cu 2p XPS spectrum revealed distinctive features, including a Cu 2p_{1/2} peak at 953.7 eV, a Cu 2p_{3/2} peak at 934.6 eV, and three supplementary satellite peaks located at 960.3, 940.5, and 937.6 eV (Fig. 3b). These supplementary peaks typically arise from an “oscillatory” mechanism where excess electrons transition to higher energy states [45]. The predominance of Cu(II) as the primary chemical state of copper on the surface of Cuf-TMB@PDA is further supported by the Auger spectrum (Fig. 3c). The C 1s spectrum exhibits peaks at 291.0, 287.6, 285.13, and 284.8 eV, corresponding to the presence of π - π^* , C–O, C–N, and C–C groups, respectively (Fig. 3d). The presence of the N 1s peak

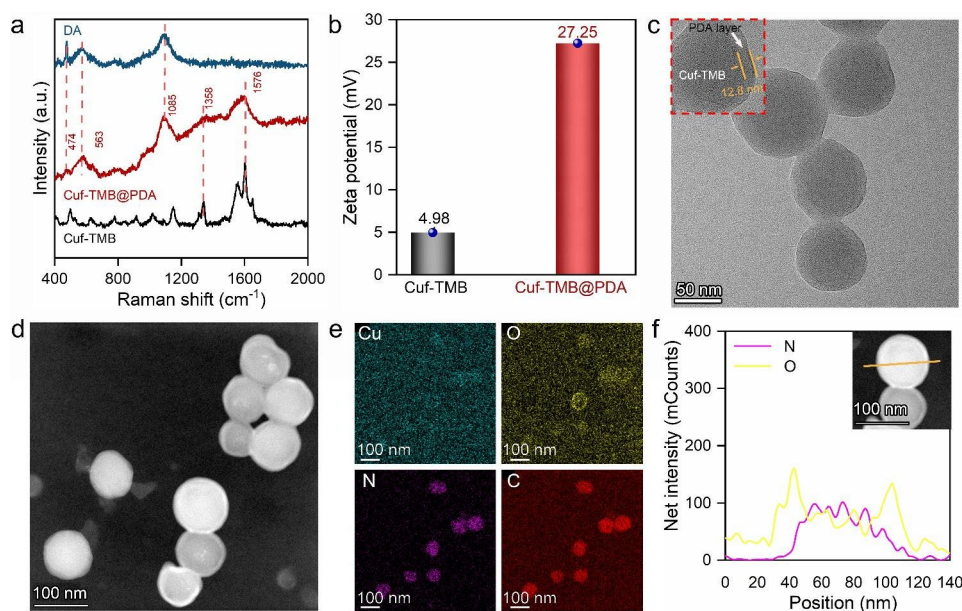


Fig. 2 Characterization of Cuf-TMB@PDA. **(a)** Raman spectra of the Cuf-TMB@PDA, Cuf-TMB, and dopamine. **(b)** Zeta potentials of the Cuf-TMB@PDA and Cuf-TMB. **(c)** Transmission electron microscope (TEM) image of Cuf-TMB@PDA (scale bar, 50 nm). **(d)** High angle annular dark field scanning transmission electron microscopy (HAADF-STEM) image. **(e)** The corresponding energy dispersive spectrometer (EDS) mapping images of Cuf-TMB@PDA (scale bar, 100 nm). **(f)** Representative EDX line scans for N and O, obtained on Cuf-TMB@PDA (orange line, scanned line)

confirmed the successful formation of the PDA shell layer, as indicated by peaks at approximately 398.4 eV, representing the presence of C-NH₂ groups. Furthermore, the N 1s XPS spectrum revealed the coexistence of Cu-N (399.5 eV), C-N (399.9 eV), and -NH₂ (401.0 eV) species (Fig. 3e). The situation with oxygen was distinct, as the local environment of oxygen experienced changes following PDA modification, which were detectable. The O 1s spectrum of Cuf-TMB@PDA showed the presence of COO⁻ (533.8 eV), C=O (532.1 eV), and Cu-O (531.1 eV) groups (Fig. 3f). Notably, the unique structure of PDA likely contributed to the elevated signal energy observed in the C-O-C group (533.0 eV) of Cuf-TMB@PDA, in contrast to the C-O-C moiety identified in Cuf-TMB (Fig. 3f, Fig. S7). These experimental findings not only verified the successful synthesis of Cuf-TMB@PDA but also provided evidence for the connection between PDA and Cuf-TMB through a robust C-O-C bond and C-NH₂ structure [46, 47].

Additionally, Cuf-TMB@PDA demonstrates a specific surface area of 101.01 cm² g⁻¹, contrasting with the 44.13 cm² g⁻¹ observed for Cuf-TMB alone. The incorporation of PDA as an encapsulating layer transforms Cuf-TMB@PDA into a core-shell structure, thereby enhancing its specific surface area Fig. S8). Notably, the POD-like activity of Cuf-TMB@PDA remains relatively stable even when exposed to a concentration of 0.1 μg mL⁻¹ dopamine (Fig. S9, Fig. S10). Optimal performance of Cuf-TMB@PDA is achieved

under conditions of 40 °C and at a specific pH level of 7 (Fig. S11).

The *in vitro* cell compatibility and hemocompatibility property of Cuf-TMB@PDA

To evaluate the biocompatibility of Cuf-TMB@PDA, cytotoxicity and hemolysis assays were explored separately. After 24 h of treatment with Cuf-TMB@PDA, a high cell viability rate (89.46%) was observed for mouse L929 cells, even at a concentration as high as 63 μg mL⁻¹, in contrast to cells treated with Cuf-TMB (63.18% viability, Fig. 4a). Furthermore, the proliferation of cells incubated in various leaching solutions with defined concentrations was assessed over a 72-hour period, revealing enhanced cell viability in the presence of Cuf-TMB@PDA leachate. In contrast, cellular activity exhibited a diminished response when exposed to Cuf and Cuf-TMB leachates, indicating the favorable cytocompatibility of the synthesized Cuf-TMB@PDA (Fig. 4b, c). To further assess cytotoxicity, cell viability was evaluated by distinguishing live L929 cells (depicted in green) from deceased cells (represented in red) using calcein-acetoxymethyl (Calcein-AM) and propidium iodide (PI). The majority of L929 cells in the Cuf-TMB@PDA-treated group demonstrated viability, confirming the improved cytocompatibility of Cuf-TMB@PDA (Fig. 4d).

Subsequently, a hemolysis examination was conducted to evaluate the hemocompatibility of the Cuf-TMB@PDA. Upon treatment with Triton, the supernatant of erythrocytes exhibited a distinct red coloration, whereas

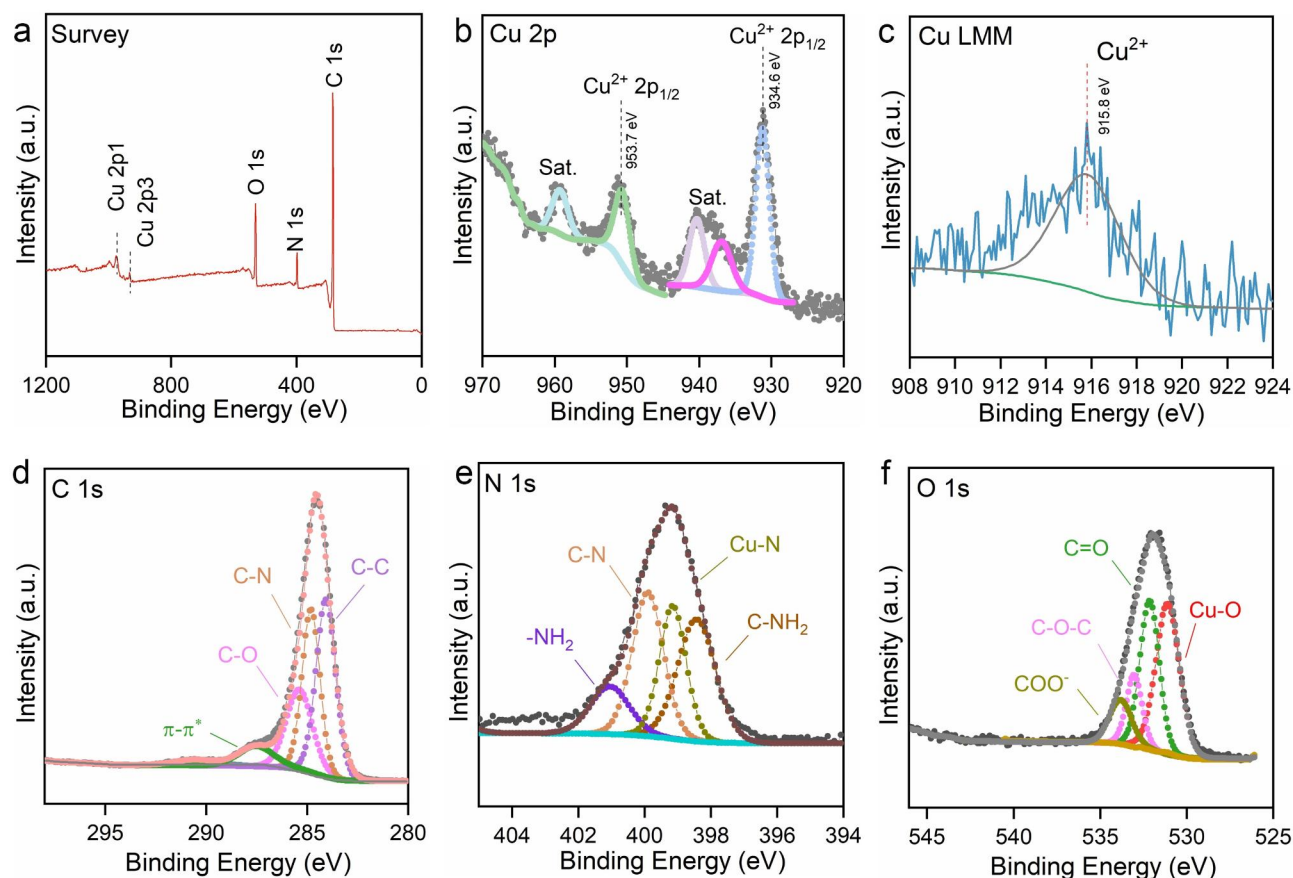


Fig. 3 The XPS spectra of Cuf-TMB@PDA. **(a)** Fully scanned XPS spectrum of Cuf-TMB@PDA; **(b)** Spectrum depicting the Cu 2p region, featuring two primary peaks and three satellite peaks; **(c)** Cu Auger spectrum of Cuf-TMB@PDA; **(d)** The C 1s spectrum of Cuf-TMB@PDA; **(e)** The N 1s spectrum; **(f)** The O 1s spectrum

the supernatants from the Cuf-TMB, Cuf-TMB@PDA, and PBS groups remained transparent and colourless (Fig. S12). These observations indicate the minimal hemolytic effect of the prepared Cuf-TMB@PDA material on erythrocytes. Collectively, these findings underscore the enhanced cytocompatibility and hemocompatibility of Cuf-TMB@PDA, thereby highlighting its potential for in vitro and in vivo wound healing applications when compared to the control groups.

In vitro antibacterial activity of Cuf-TMB@PDA

The antibacterial efficacy of Cuf-TMB@PDA was firstly evaluated in vitro. At a concentration of $63 \mu\text{g mL}^{-1}$, Cuf-TMB@PDA demonstrated significant bactericidal activity against both *E. coli* and *S. aureus*. After 24 h of co-incubation, the survival rate of *E. coli* was reduced to 0.57%, and that of *S. aureus* was reduced to 2.43%. This concentration was determined as the optimal dose of Cuf-TMB@PDA to achieve the desired bactericidal effect (Fig. 5a). Moreover, a bacteriostatic assessment was conducted over a continuous 72-hour period for PBS, PDA, Cuf, Cuf-TMB, and Cuf-TMB@PDA. The PDA treated group showed a gradual emergence of antibacterial

activity exhibited by PDA over time. This phenomenon can be attributed to the positive charge on the surface of PDA, which promotes prolonged adherence to bacterial surfaces. Consequently, this disrupts bacterial nutrient absorption, ultimately resulting in bacterial mortality (Fig. 5b, Fig. S13). The concentrations of Cuf and Cuf-TMB were determined based on the copper content in Cuf-TMB@PDA, with a concentration of $6.55 \mu\text{g mL}^{-1}$ of Cu(II). Both Cuf and Cuf-TMB demonstrated significant bactericidal efficacy, achieving 99.17% and 99.58% bacterial eradication, respectively, after 24-hour treatment. No bacterial colonies of *E. coli* and *S. aureus* were observed in the Cuf, Cuf-TMB, and Cuf-TMB@PDA groups throughout the 72-hour duration on the agar plate. This observation indicates that both Cuf-TMB and Cuf-TMB@PDA exhibited potent antibacterial activity, which can be attributed to the presence of Cu(II) ions and free radicals.

To further investigate the bactericidal mechanism of Cuf-TMB@PDA, the absorbance values at $\text{OD}_{260 \text{ nm}}$ of various incubation groups were recorded. The OD values of Cuf-TMB@PDA, Cuf, and Cuf-TMB exhibited significantly higher levels compared to those of the control

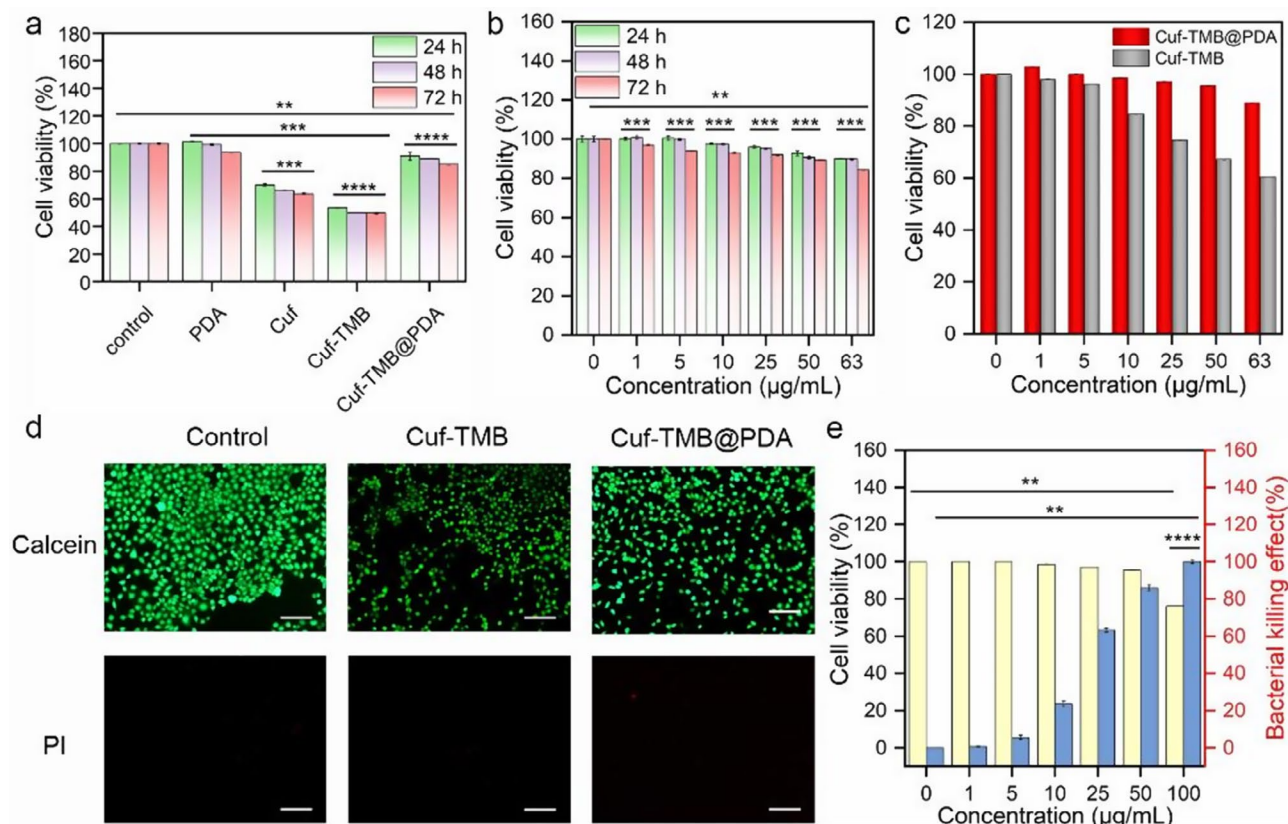


Fig. 4 Evaluation of the cytocompatibility of Cuf-TMB@PDA. **(a)** The viability of L929 cells was examined after exposure to various treatments for durations of 24, 48, and 72 h, respectively. **(b)** Viability of L929 cells after incubation in leaching solutions with different concentrations for 24 h, 48 h, and 72 h. **(c)** Viability of L929 cells after incubation in leaching solutions with varying concentrations of Cuf-TMB@PDA and Cuf-TMB for 24 h. **(d)** Live/dead staining results of L929 cells following incubation in the leaching solution of Cuf-TMB@PDA ($63 \mu\text{g mL}^{-1}$) for 24 h (scale bar: 200 μm). **(e)** Determination of the optimal Cuf-TMB@PDA concentration for both cell cytocompatibility and antibacterial activity (* $P < 0.05$, ** $P < 0.01$, *** $P < 0.001$)

groups. This confirmed the ability of Cuf, Cuf-TMB, and Cuf-TMB@PDA, all containing Cu(II), to induce disruption of the bacterial membrane. Consequently, this led to the release and detectability of its contents (Fig. 5c). In addition, bacterial lipid peroxidation was notably prominent in the Cuf-TMB@PDA, Cuf-TMB, and Cuf-treated groups, which aligns with the previously mentioned antibacterial activities (Fig. 5d).

Bacterial resistance often arises as a result of bacterial biofilm presence, and targeting these biofilms remains an effective strategy for combating bacterial infections. Bacterial biofilms possess the ability to offer protection against external threats, thereby reducing the effectiveness of nanoparticles in antibacterial applications. Therefore, effectively inhibiting biofilm formation has the potential to enhance antibacterial efficacy. To assess the inhibition of biofilm growth, crystal violet staining was employed to quantify the biofilm masses. In all groups containing Cu(II), a noticeable decrease in the rate of biofilm formation was observed, indicating their inhibitory effect on biofilm growth (Fig. 5f, Fig. S14). It is

noteworthy to mention that PDA alone exhibited a lesser impact on biofilm formation.

For a deeper understanding of the antimicrobial mechanisms, we conducted SEM measurements to examine the cellular morphology of the bacteria treated with these compounds. In the control-treated groups, the cell membranes of *S. aureus* and *E. coli* remained intact and smooth. However, in the groups treated with Cuf-TMB and Cuf-TMB@PDA, we observed the presence of some noticeable wrinkles on the cell membranes. This observation suggests the antimicrobial effect of Cuf-TMB and Cuf-TMB@PDA in compromising the integrity of bacterial cell membranes (Fig. 5g). Furthermore, certain cell membranes were severely compromised, leading to the release of cytoplasm from within the bacterial cells. Additionally, we performed a comparative analysis to evaluate the antimicrobial properties of traditional antimicrobial materials, including TiO_2 nanoparticles, Ag nanoparticles, and vancomycin antibiotics. The antimicrobial capabilities demonstrated by both Cuf-TMB@PDA and Cuf-TMB are comparable to antibiotics and significantly

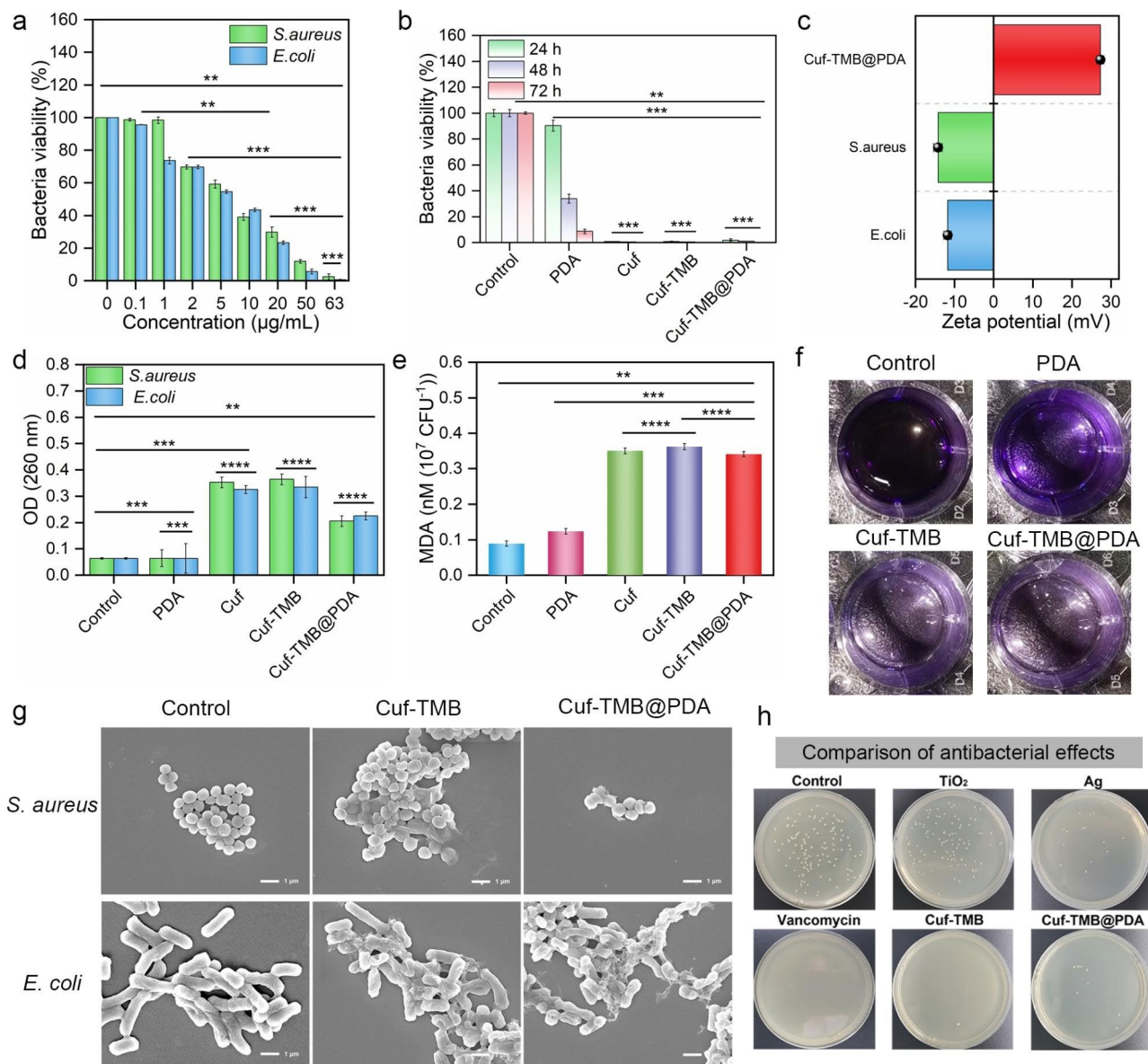


Fig. 5 In vitro evaluation of the antimicrobial performance of Cuf-TMB@PDA. **(a)** The inhibitory effect of bacteria after 24-hour incubation in leaching solutions with varying concentrations. **(b)** The inhibition property of *E. coli* after subjecting them to different treatments for 24, 48, and 72 h. **(c)** The zeta potential of Cuf-TMB@PDA in relation to several bacterial zeta potentials. **(d)** OD_{260 nm} of *E. coli* and *S. aureus* treated with PBS, PDA, Cuf, Cuf-TMB, and Cuf-TMB@PDA. **(e)** The MDA level in *E. coli* and *S. aureus* under different treatment conditions. **(f)** Photographs of crystalline violet-stained biofilms after various treatments. **(g)** SEM images of *E. coli* and *S. aureus* incubated with PBS, Cuf-TMB, Cuf-TMB@PDA, respectively. **(h)** The antibacterial ratio of different samples, including TiO₂, Ag, vancomycin, Cuf-TMB, and Cuf-TMB@PDA, against *E. coli* using the agar plating method (* $P < 0.05$, ** $P < 0.01$, *** $P < 0.001$)

surpass the performance of conventional synthetic antimicrobial materials (Fig. 5h, Fig. S15).

In order to investigate the antibacterial mechanism, we utilized ESR to detect free radicals in Cuf-TMB and Cuf-TMB@PDA (Fig. S16). Comparatively, Cuf-TMB@PDA exhibited a diminished intensity of $\cdot\text{OH}$ radicals when compared to Cuf-TMB. This reduction in intensity can be attributed to the depletion of radicals during the polymerization process of dopamine into polydopamine. The presence of residual free radicals in the Cuf-TMB@PDA

system was confirmed through ESR analysis. These free radicals have the potential to induce peroxidation within the bacterial cells, augmenting the antimicrobial effect by synergizing with Cu(II) and exerting a bactericidal effect. These results validate the remarkable bactericidal properties and superior biocompatibility of the antibacterial platform, Cuf-TMB@PDA, making it a promising candidate for in vivo applications.

In vivo wound healing of Cuf-TMB@PDA

To further validate the in vivo antibacterial efficacy, a mouse wound infection model was employed as a proof of concept. The mice were divided into three groups, each receiving different treatments: (1) PBS; (2) Cuf-TMB; and (3) Cuf-TMB@PDA. The antimicrobial effect was evaluated by monitoring wound size at 1, 3, 5, and 7 days, along with the quantification of bacterial counts within the wounds (Fig. 6a). Additionally, the presence of bacteria at the wound sites was assessed using the agar plate method to determine the bactericidal effect Fig. S17). As anticipated, both the Cuf-TMB and Cuf-TMB@PDA groups exhibited minimal bacterial growth on the agar plates, which aligned with the results obtained from the in vitro experiments. Schematic illustrations depicting wound contraction and the calculation of wound

contraction were also provided in Fig. 6b. Notably, after 7 days of treatment, the wound treated with Cuf-TMB@PDA presented the smallest proportion of open wound area (10.63%) and displayed a smoother appearance with the presence of newly formed epidermal and dermal tissues. In contrast, the Cuf-TMB and PBS groups exhibited open wound areas of 19.99% and 20.79%, respectively, accompanied by visibly uneven scar tissue. These findings strongly highlight the superior wound healing efficacy of the Cuf-TMB@PDA group compared to the other treatment groups.

To affirm the observed healing outcomes, a comprehensive evaluation of wound healing was conducted by examining histological changes in the skin tissue. Upon completion of the treatment period, the mice were sacrificed at specific time intervals, and tissue samples were

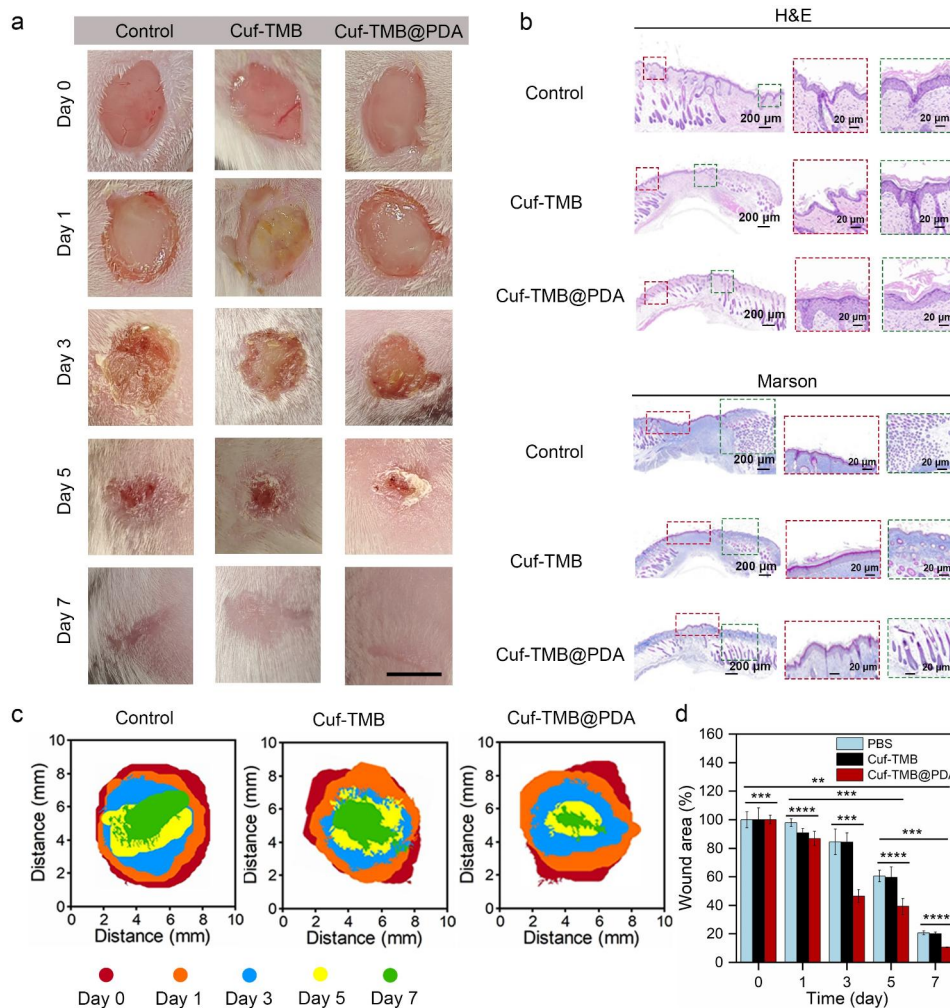


Fig. 6 In vivo wound closure assessment of Cuf-TMB@PDA. **(a)** Photographs captured at various time points (0, 1, 3, 5, and 7 days) to visually document the progress of wound healing with different dressings. Each photograph was accompanied by a 10 mm scale bar. **(b)** H&E stained sections analyzed on the 7th day of the wound healing models. The red box represents the newly formed granulation tissue, while the green box indicates the presence of hair follicles. **(c)** Masson's trichrome stained sections were utilized to detect collagen (shown as blue staining). **(d)** Schematic images of wound contraction during 7 days for the treatments by PBS, Cuf-TMB, and Cuf-TMB@PDA. Wound area for each group (n = 3). **(e)** Corresponding wound area recorded at various time points to assess the progression of healing (**P* < 0.05, ***P* < 0.01, ****P* < 0.001)

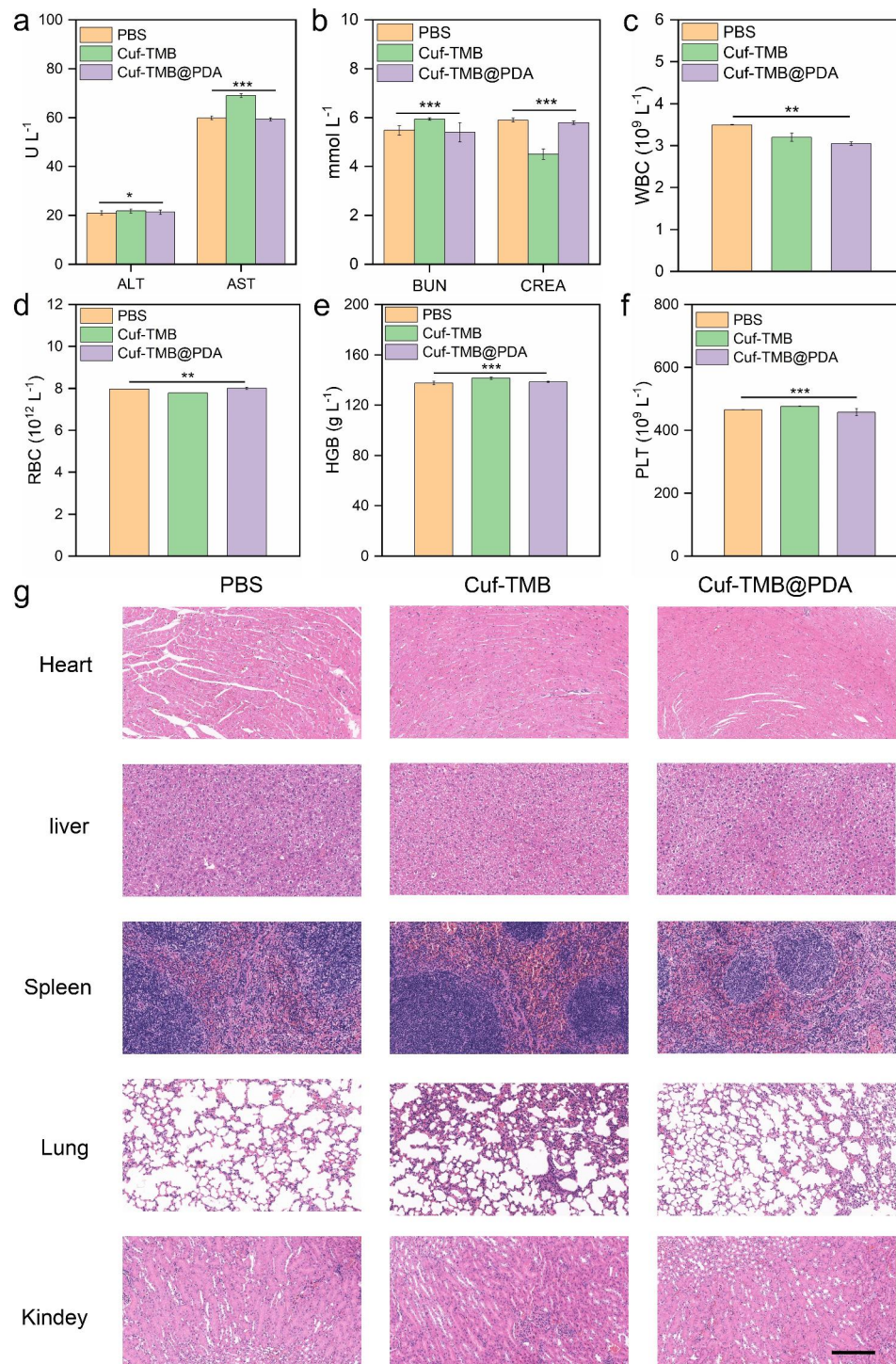


Fig. 7 Biosafety evaluation of Cuf-TMB@PDA. **(a)** Liver function test of alanine aminotransferase (ALT) and aspartate aminotransferase (AST). **(b)** Kidney function test of blood urea nitrogen (BUN) and creatinine (CREA). **(c)–(f)** Blood analysis of mice after exposing to different materials after 7 days, respectively. **(c)** Total white blood cell (WBC), **(d)** total red blood cells (RBC), **(e)** hemoglobin (HGB) and **(f)** blood platelet (PLT) counts (* $P < 0.05$, ** $P < 0.01$, *** $P < 0.001$). **(g)** H&E staining of the heart, liver, spleen, lung, and kidney with different treatments after 7 days (scale bar: 200 μm)

collected for analysis. H&E staining, as well as Masson staining, were utilized to evaluate the *in vivo* wound healing efficacy of Cuf-TMB and Cuf-TMB@PDA. At the 7th day, a notable abundance of granulation tissue was

observed in the Cuf-TMB@PDA group, surpassing the other groups (Fig. 6c). The H&E staining results revealed that the scar width in the Cuf-TMB@PDA-treated group (1.15 mm) was significantly smaller compared to the PBS

(5.59 mm) and Cuf-TMB (1.52 mm) groups. Additionally, upon closer examination of the H&E images, the Cuf-TMB@PDA-treated skin tissue exhibited reduced inflammatory signals (blood cells and neutrophils), increased collagen fibers, and visible dermal tissue, including hair follicle appendages, among other characteristics. During the maturation phase of wound repair, collagen deposition plays a critical role in scar formation, while wound contraction is facilitated by the interconnection of fibroblasts and collagen. The accumulation of newly formed collagen in the regenerated skin tissue was evident through Masson staining. Notably, the Cuf-TMB@PDA group demonstrated elevated levels of collagen deposition at the wound edges compared to the control group. Similarly, the analysis of kidney and liver function did not demonstrate any toxicity within the organism (Fig. 7a and b). Other blood parameters, such as white blood cell (WBC), red blood cells (RBC), hemoglobin (HGB) and blood platelet (PLT), fell within the normal range (Fig. 7c and f). Moreover, H&E staining revealed that Cuf-TMB@PDA did not induce any damage or toxicity to the normal anatomical structures of diverse organs throughout the treatment duration (Fig. 7a g). Hence, Cuf-TMB@PDA treatment has no toxic effect on the circulatory system of organisms. All these results strongly supported that the potential of Cuf-TMB@PDA as a promising candidate for wound healing purposes.

Conclusions

To summarize, our study introduced an antimicrobial agent called Cuf-TMB@PDA, which was applied to investigate the healing of skin wounds in mice. Unlike previously reported copper-based antimicrobial materials that exhibited significant cytotoxicity, Cuf-TMB@PDA demonstrated enhanced antibacterial efficacy without compromising cytocompatibility. The positive charge of Cuf-TMB@PDA enables it to effectively trap and interact with negatively charged bacteria through electrostatic adsorption. This close interaction exposes the bacteria to the encapsulated free radicals within Cuf-TMB@PDA, leading to oxidative damage and the concurrent release of Cu(II) within an optimal range. These combined mechanisms greatly enhance the antibacterial effectiveness of Cuf-TMB@PDA. Importantly, our findings indicate that Cuf-TMB@PDA exhibits low toxicity in complex settings. With its dual attributes of antimicrobial effectiveness and cytocompatibility, Cuf-TMB@PDA holds significant potential for applications in skin tissue repair, providing inherent anti-infective protection.

Supplementary Information

The online version contains supplementary material available at <https://doi.org/10.1186/s12951-023-02247-w>.

Supplementary Material 1: Experimental Section; Scheme S1.

Dopamine undergoes polymerization in the presence of free radicals, resulting in the formation of polydopamine. **Fig. S1.** The FT-IR spectra of Cuf-TMB@PDA and Cuf-TMB. **Fig. S2.** Zeta potentials of Cuf-TMB@PDA NPs using different concentrations of dopamine. **Fig. S3.** XRD pattern of Cuf-TMB@PDA and Cuf-TMB. **Fig. S4.** (a) The SAED pattern of Cuf-TMB NPs. (b) HRTEM image of Cuf-TMB NPs. (c) The SAED pattern of Cuf-TMB@PDA. (d) HRTEM image of Cuf-TMB@PDA. **Fig. S5.** SEM images of (a) Cuf-TMB and (b) Cuf-TMB@PDA. **Fig. S6.** The Energy Dispersive X-Ray Spectroscopy (EDX) mapping of Cuf-TMB. **Fig. S7.** Fine XPS spectra of Cuf-TMB NPs: (a) Cu 2p; (b) C 1s; (c) N 1s; (d) O 1s. **Fig. S8.** The Brunauer-Emmett-Teller (BET) characterization of Cuf-TMB@PDA and Cuf-TMB. **Fig. S9.** (a) Reaction-time curves of TMB colorimetric reactions catalyzed by Cuf-TMB@PDA. (b) Comparison of the specific activities of Cuf-TMB@PDA using different concentrations of dopamine. **Fig. S10.** (a)-(g) Comparison of particle size for Cuf-TMB coated with varying concentrations of dopamine. **Fig. S11.** (a) Effect of pH value on the POD-like activity of Cuf-TMB@PDA. (b) Effect of temperature on the POD-like activity of Cuf-TMB@PDA. **Fig. S12.** (a) Evaluation of hemocompatibility of different concentrations of Cuf-TMB@PDA. (b) Hemocompatibility Evaluation, Triton X-100, PBS, Cuf-TMB, Cuf-TMB@PDA. **Fig. S13.** Comparison of the inhibition effect of Cuf-TMB@PDA acting on bacteria (*E. coli* and *S. aureus*). **Fig. S14.** The growth curves of (a) *E. coli* and (b) *S. aureus* after incubation with different concentrations (from 0 to 63 $\mu\text{g mL}^{-1}$) of Cuf-TMB@PDA. **Fig. S15.** Evaluation of the antimicrobial activities of TiO₂, Ag, vancomycin antibiotic, Cuf-TMB, and Cuf-TMB@PDA. **Fig. S16.** The ESR spectra of Cuf-TMB@PDA and Cuf-TMB. **Fig. S17.** Representative photographs of bacterial cultures taken from *S. aureus* infected wound areas at different times during the treatment phase. **Fig. S18.** Dynamic body weight changes of *S. aureus* infected rats in various groups over 7 days. **Tab. S1.** Analysis of FTIR spectra of Cuf-TMB@PDA NPs. **Tab. S2.** Elemental analysis of Cuf-TMB and Cuf-TMB@PDA.

Acknowledgements

Not applicable.

Author Contributions

J.P. and Y.Z. contributed to the design and completion of the study; J.P., P.S., Y.C. and J.Y. made contributions in experiments and guided the data analysis; Q.W. and J.P. participated in manuscript revision. All authors read and approved the final manuscript.

Funding

This work was supported by the National Natural Science Foundation of China (Grant No. 21905237 and 82302275), the Fundamental Research Funds for the Central Universities (WUT: 2022IVA160 and 2022IVA089), the Young Top-notch Talent Cultivation Program of Hubei Province (Grant No. 40129014), China Postdoctoral Science Foundation (Grant No. 2017M612131), the 7th Yong elite scientist sponsorship program by CAST (No. YESS20210191), and the National Key Research and Development (R&D) Program of Chian (Grant NO. 2018YFB1105702).

Data Availability

All data generated or analyzed during this are included in this paper.

Declarations

Ethics approval and consent to participate

All animal experiments were carried out in accordance with Wuhan University of Technology's animal care and experiment rules.

Consent for publication

All authors agree to be published.

Competing interests

The authors declare no competing interests.

Received: 17 October 2023 / Accepted: 3 December 2023

Published online: 10 December 2023

References

- Levy SB, Marshall B. Antibacterial resistance worldwide: causes, challenges and responses. *Nat Med*. 2004;10(12):122–5129.
- Chen S, Lu J, You T, Sun D. Metal-organic frameworks for improving wound healing. *Coord Chem Rev*. 2021;439:213929.
- Zhong Y, Zheng XT, Zhao S, Su X, Loh XJ. Stimuli-activable metal-bearing nanomaterials and precise on-demand antibacterial strategies. *ACS Nano*. 2022;16(12):19840–72.
- Jin J, Mangal U, Seo JY, Kim JY, Ryu JH, Lee YH, Lugtu C, Hwang G, Cha JY, Lee KJ, Yu HS, Kim KM, Jang S, Kwon JS, Choi SH. Cerium oxide nanozymes confer a cytoprotective and bio-friendly surface micro-environment to methacrylate based oro-facial prostheses. *Biomaterials*. 2023;296:122063.
- Li J, Xia Q, Guo H, Fu Z, Liu Y, Lin S, Liu J. Decorating bacteria with triple immune nanoactivators generates tumor-resident living immunotherapeutics. *Angew Chem Int Ed*. 2022;61(27):e202202409.
- Wang Y, Yang Y, Shi Y, Song H, Yu C. Antibiotic-free antibacterial strategies enabled by nanomaterials: progress and perspectives. *Adv Mater*. 2020;32(18):e1904106.
- Liang Y, Li Z, Huang Y, Yu R, Guo B. Dual-dynamic-bond cross-linked antibacterial adhesive hydrogel sealants with on-demand removability for post-wound-closure and infected wound healing. *ACS Nano*. 2021;15(4):7078–93.
- Li J, Li Z, Liu X, Li C, Zheng Y, Yeung KWK, Cui Z, Liang Y, Zhu S, Hu W, Qi Y, Zhang T, Wang X, Wu S. Interfacial engineering of Bi₂S₃/Ti₃C₂T_x MXene based on work function for rapid photo-excited bacteria-killing. *Nat Commun*. 2021;12(1):1224.
- Lu X, Chen R, Lv J, Xu W, Chen H, Ma Z, Huang S, Li S, Liu H, Hu J, Nie L. High-resolution bimodal imaging and potent antibiotic/photodynamic synergistic therapy for osteomyelitis with a bacterial inflammation-specific versatile agent. *Acta Biomater*. 2019;99:363–72.
- Wu Z, Duan F, Zhang J, Li S, Ma H, Nie L. *In vivo* dual-scale photoacoustic surveillance and assessment of burn healing. *Biomed Opt Express*. 2019;10(7):3425–33.
- Zhou Z, Li S, Wei G, Liu W, Zhang Y, Zhu C, Liu S, Li T, Wei H. Cerium-based metal-organic framework with intrinsic haloperoxidase-like activity for antibiofilm formation. *Adv Funct Mater*. 2022;32(39):2206294.
- Gholami Derami H, Gupta P, Weng KC, Seth A, Gupta R, Silva JR, Raman B, Singamaneni S. Reversible photothermal modulation of electrical activity of excitable cells using polydopamine nanoparticles. *Adv Mater*. 2021;33(32):e2008809.
- Nudelman R, Gavriely S, Bychenko D, Barzilay M, Gulakhmedova T, Gazit E, Richter S. Bio-assisted synthesis of bimetallic nanoparticles featuring antibacterial and photothermal properties for the removal of biofilms. *J Nanobiotechnol*. 2021;19(1):452.
- Zhao P, Feng Y, Zhou Y, Tan C, Liu M. Gold@Halloysite nanotubes-chitin composite hydrogel with antibacterial and hemostatic activity for wound healing. *Bioact Mater*. 2023;20:355–67.
- Yang G, Zhang Z, Liu K, Ji X, Fatehi P, Chen J. A cellulose nanofibril-reinforced hydrogel with robust mechanical, self-healing, pH-responsive and antibacterial characteristics for wound dressing applications. *J Nanobiotechnol*. 2022;20(1):312.
- Peng Y, Liu Y, Lu X, Wang S, Chen M, Huang W, Wu Z, Lu G, Nie L. Ag-Hybridized plasmonic Au-triangular nanoplates: highly sensitive photoacoustic/Raman evaluation and improved antibacterial/photothermal combination therapy. *J Mater Chem B*. 2018;6(18):2813–20.
- Zha K, Xiong Y, Zhang W, Tan M, Hu W, Lin Z, Cheng P, Lu L, Cai K, Mi B, Feng Q, Zhao Y, Liu G. Waste to wealth: near-infrared/pH dual-responsive copper-humic acid hydrogel films for bacteria-infected cutaneous wound healing. *ACS Nano*. 2023;17(17):17199–216.
- Guo Y, Xie B, Jiang M, Yuan L, Jiang X, Li S, Cai R, Chen J, Jiang X, He Y, Tao G. Facile and eco-friendly fabrication of biocompatible hydrogel containing CuS@Ser NPs with mechanical flexibility and photothermal antibacterial activity to promote infected wound healing. *J Nanobiotechnol*. 2023;21(1):266.
- Zheng Z, Liang W, Lin R, Hu Z, Wang Y, Lu H, Zhong W, Shen S, Pan Y. Facile synthesis of zinc indium oxide nanofibers distributed with low content of silver for superior antibacterial activity. *Small*. 2023;4(4):2200291.
- Qi X, Huang Y, You S, Xiang Y, Cai E, Mao R, Pan W, Tong X, Dong W, Ye F, Shen J. Engineering robust ag-decorated polydopamine nano-photothermal platforms to combat bacterial infection and prompt wound healing. *Adv Sci*. 2022;9(11):e2106015.
- Wang H, Wu Y, Zou H, Song Z, Wang Y, Wang H, Zhou M. Photothermal therapy with Ag nanoparticles in mesoporous polydopamine for enhanced antibacterial activity. *ACS Appl Nano Mater*. 2023;6(6):4834–43.
- Li Y, Liu X, Tan L, Cui Z, Yang X, Zheng Y, Yeung KWK, Chu PK, Wu S. Rapid sterilization and accelerated wound healing using Zn²⁺ and graphene oxide modified g-C₃N₄ under dual light irradiation. *Adv Funct Mater*. 2018;28(30):1800299.
- Li M, Gao L, Schlaich C, Zhang J, Donskyi IS, Yu G, Li W, Tu Z, Rolff J, Schwerdtle T, Haag R, Ma N. Construction of functional coatings with durable and broad-spectrum antibacterial potential based on mussel-inspired dendritic polyglycerol and in situ-formed copper nanoparticles. *ACS Appl Mater Interfaces*. 2017;9(40):35411–8.
- Peter T, Shannon C, Boryana P, Margaret D, Ana V, Mai A, Jordan R, Lena J-C, Ranad H, Ryan DS, John KE, Evgeni F, Mustafa K, Steven M, Svetlana L, Naama K, Sandro S, Golub TR. Copper induces cell death by targeting lipoylated Tca cycle proteins. *Science*. 2022;375:1254–61.
- Xiao J, Zhu Y, Huddleston S, Li P, Xiao B, Farha OK, Ameer GA. Copper metal-organic framework nanoparticles stabilized with folic acid improve wound healing in Diabetes. *ACS Nano*. 2018;12(2):1023–32.
- Giacomelli C, Trincavelli ML, Satriano C, Hansson O, La Mendola D, Rizzarelli E, Martini C. Copper (II) ions modulate angiogenin activity in human endothelial cells. *Int J Biochem Cell Biol*. 2015;60:185–96.
- Boyer C, Corrigan NA, Jung K, Nguyen D, Nguyen T-K, Adnan NNM, Oliver S, Shanmugam S, Yeow J. Copper-mediated living radical polymerization (atom transfer radical polymerization and copper(0) mediated polymerization): from fundamentals to bioapplications. *Chem Rev*. 2015;116(4):1803–949.
- Guo C, Cheng F, Liang G, Zhang S, Jia Q, He L, Duan S, Fu Y, Zhang Z, Du M. Copper-based polymer-metal-organic framework embedded with ag nanoparticles: long-acting and intelligent antibacterial activity and accelerated wound healing. *Chem Eng J*. 2022;435:134915.
- Qu WQ, Fan JX, Zheng DW, Gu HY, Yu YF, Yan X, Zhao K, Hu ZB, Qi BW, Zhang XZ, Yu AX. Deep-penetration functionalized cuttlefish ink nanoparticles for combating wound infections with synergetic photothermal-immunologic therapy. *Biomaterials*. 2023;301:122231.
- Yu S, Li G, Liu R, Ma D, Xue W. Dendritic Fe₃O₄@Poly(dopamine)@PAMAM nanocomposite as controllable no-releasing material: a synergistic photothermal and no antibacterial study. *Adv Funct Mater*. 2018;28(20):1707440.
- Barclay TG, Hegab HM, Clarke SR, Ginic-Markovic M. Versatile surface modification using polydopamine and related polycatecholamines: Chemistry, structure, and applications. *Adv Mater Interfaces*. 2017;4(19):1601192.
- Liu S, Zhang C, Zhou Y, Zhang F, Duan X, Liu Y, Zhao X, Liu J, Shuai X, Wang J, Cao Z. MRI-visible mesoporous polydopamine nanoparticles with enhanced antioxidant capacity for osteoarthritis therapy. *Biomaterials*. 2023;295:122030.
- Mohandas A, Deepthi S, Biswas R, Jayakumar R. Chitosan based metallic nanocomposite scaffolds as antimicrobial wound dressings. *Bioact Mater*. 2018;3(3):267–77.
- Liu M, Huang L, Xu X, Wei X, Yang X, Li X, Wang B, Xu Y, Li L, Yang Z. Copper doped carbon dots for addressing bacterial biofilm formation, wound infection, and tooth staining. *ACS Nano*. 2022;16(6):9479–97.
- Lin S, Cheng Y, Zhang H, Wang X, Zhang Y, Zhang Y, Miao L, Zhao X, Wei H. Copper tannic acid coordination nanosheet: a potent nanozyme for scavenging ros from cigarette smoke. *Small*. 2020;16(27):e1902123.
- Qazi TH, Mooney DJ, Pumberger M, Geißler S, Duda GN. Biomaterials based strategies for skeletal muscle tissue engineering: existing technologies and future trends. *Biomaterials*. 2015;53:502–21.
- Lu L, Zhang J, Guan K, Zhou J, Yuan F, Guan Y. Artificial neural network for cytocompatibility and antibacterial enhancement induced by femtosecond laser micro/nano structures. *J Nanobiotechnol*. 2022;20(1):365.
- Sun X, Dong M, Guo Z, Zhang H, Wang J, Jia P, Bu T, Liu Y, Li L, Wang L. Multifunctional chitosan-copper-gallic acid based antibacterial nanocomposite wound dressing. *Int J Biol Macromol*. 2021;167:10–22.
- Xu P, Huang W, Yang J, Fu X, Jing W, Zhou Y, Cai Y, Yang Z. Copper-rich multifunctional prussian blue nanozymes for infected wound healing. *Int J Biol Macromol*. 2023;227:1258–70.
- Rivera LR, Cochis A, Biser S, Canciani E, Ferraris S, Rimondini L, Boccaccini AR. Antibacterial, pro-angiogenic and pro-osteointegrative zein-bioactive glass/copper based coatings for implantable stainless steel aimed at bone healing. *Bioact Mater*. 2021;6(5):1479–90.
- He S, Feng Y, Sun Q, Xu Z, Zhang W. Charge-switchable Cu₂O nanozyme with peroxidase and near-infrared light enhanced photothermal activity for wound antibacterial application. *ACS Appl Mater Interfaces*. 2022;14(22):25042–9.

42. Zhou Y, Chen X, Zhan S, Wang Q, Deng F, Wu Q, Peng J. Stabilized and controlled release of radicals within copper formate-based nanozymes for biosensing. *ACS Appl Mater Interfaces*. 2023;15(37):43431–40.
43. Xue Y, Niu W, Wang M, Chen M, Guo Y, Lei B. Engineering a biodegradable multifunctional antibacterial bioactive nanosystem for enhancing Tumor photothermo-chemotherapy and bone regeneration. *ACS Nano*. 2019;14(1):442–53.
44. Tong C, Zhong X, Yang Y, Liu X, Zhong G, Xiao C, Liu B, Wang W, Yang X. PB@PDA@Ag nanosystem for synergistically eradicating MRSA and accelerating diabetic wound healing assisted with laser irradiation. *Biomaterials*. 2020;243:119936.
45. Castle JE. Use of shake-up satellites in Photoelectron Spectra for analysis of oxide layers on metals. *Nat Phys*. 1971;234:93–5.
46. Zeng Y, Sun PX, Pei Z, Jin Q, Zhang X, Yu L, Lou XWD. Nitrogen-doped carbon fibers embedded with zincophilic Cu nanoboxes for stable Zn-metal anodes. *Adv Mater*. 2022;34(18):e2200342.
47. Cheng S, Qi M, Li W, Sun W, Li M, Lin J, Bai X, Sun Y, Dong B, Wang L. Dual-responsive nanocomposites for synergistic Antibacterial therapies facilitating Bacteria-infected Wound Healing. *Adv Healthc Mater*. 2023;12(6):e2202652.

Publisher's Note

Springer Nature remains neutral with regard to jurisdictional claims in published maps and institutional affiliations.